Journal of Science and Technology in Civil Engineering, HUCE, 2026, 20 (1): 80–99

# A RITZ SOLUTION FOR COMPREHENSIVE ANALYSIS OF FUNCTIONALLY GRADED BEAMS WITH VARIOUS BOUNDARY CONDITIONS

Ngoc-Duong Nguyen[a,*]

[a]*Faculty of Civil Engineering, Ho Chi Minh City University of Technology and Engineering, No. 1 Vo Van Ngan street, Thu Duc ward, Ho Chi Minh city, Vietnam*

***Article history:***
*Received 15/10/2025, Revised 13/12/2025, Accepted 27/1/2026*

**Abstract**

The present study applies a Ritz solution that employs Laguerre polynomials to comprehensively analyse functionally graded beams characterised by varying material properties across their thickness. The material distribution within the beams follows a power-law relationship, indicating a continuous variation in the material distribution throughout the beams. Furthermore, the beam displacement is established using the higher-order shear deformation theory, and the governing equation is formulated based on the Lagrange equation. Various typical boundary conditions, including clamped-clamped, clamped-simply supported, clamped-free, and simply-supported, are considered. The proposed method is validated through numerical simulations, shedding light on the influence of boundary conditions, power-law exponents, and slenderness on the buckling, free vibration, and bending behaviours of functionally graded beams.

*Keywords:* functionally graded beams; bending; buckling; free vibration; Ritz method.

https://doi.org/10.31814/stce.huce2026-20(1)-06 

## 1. Introduction

In numerous research and development endeavours, engineers commonly face a paramount challenge: selecting materials that can meet both the technical and economic requirements concurrently. To address this concern, a cadre of Japanese scientists has introduced an innovative, functionally graded (FG) material designed to fabricate thermal barriers capable of withstanding elevated surface temperatures and enduring harsh operational conditions [1]. FG materials are classifiable as advanced materials characterised by a continuous variation of material properties along specified dimensions. Compared to traditional composites, the utility of these materials is discernible in their capacity to mitigate issues such as stress concentration, fracturing, and interfacial complications. Notably, FG materials have been found to be applicable across various engineering domains, encompassing military, aerospace, biomedical, nuclear, and electrical engineering [2]. The widespread application of FG materials has attracted the attention of scientists who are constantly seeking the most accurate and cost-effective methods to analyse these structures. Therefore, studying methods is an exciting research direction when examining the FG structures [3–5].

The finite element method (FEM) has garnered substantial recognition as the method of choice for the analysis of FG structures and some of the research mentioned here. Vo et al. [6] utilised the FEM along with higher-order shear deformation theory (HSDT) to investigate the buckling and free vibration responses of FG sandwich beams. Kahya and Turan [7] developed the FEM in conjunction with the first-order shear deformation theory (FSDT) to study free vibration and stability phenomena in

*Corresponding author. *E-mail address:* duongnn@hcmute.edu.vn (Nguyen, N.-D.)

FG sandwich beams. The buckling response of FG sandwich beams using a combination of FEM and layer-wise theory is investigated by Liu et al. [8]. Pham [9] assessed the bending characteristics of FG sandwich beams utilising FSDT and FEM. Belarbi et al. [10] proposed a refined HSDT combined with FEM for analysing FG sandwich curved beams. Additionally, Garg et al. [11] investigated the bending response of FG sandwich beams under hygro-thermo-mechanical loading conditions using FEM along with HSDT. Benzid and Tati [12] introduced a two-node FEM for analysing FG beams based on the Timoshenko beam theory. The buckling response of FG beams based on a third-order zigzag theory and FEM is examined by Gupta and Chalak [13]. Recently, Mesbah et al. [14] investigated the free vibration and stability behaviours of FG beams using the FEM and a quasi-three-dimensional theory.

In addition to the FEM, the meshless method is also employed for analysing FG beams. Sayyidmousavi et al. [15] predicted the dynamic response of FG sandwich beams using the meshless method. Li et al. [16] introduced a novel meshless model for the bending analysis of bi-directional FG beams based on the third-order Reddy-Bickford theory. Ahmadi [17] proposed a meshless method to investigate the dynamic behaviour of bi-directional FG nanobeams by integrating the FSDT and the nonlocal theory of elasticity. Jiao et al. [18] conducted free vibration and buckling analyses of FG beams utilising the dual mesh control domain method based on Euler-Bernoulli and Timoshenko beam models.

Furthermore, the iso-geometric method has garnered the attention of researchers. Rahmani et al. [19] investigated the vibration and bending characteristics of metallic and FG beam structures using Carrera unified formulation and iso-geometric analysis. Dinachandra and Alankar [20] presented the static and dynamic modeling of FG- microbeams using strain gradient theories. Chen et al. [21] demonstrated a free vibration analysis of FG microbeams based on the Timoshenko beam theory, the modified couple stress theory, and iso-geometric analysis.

In addition to numerical methods, analytical methods have garnered attention from researchers due to their advantages, including providing insights into problems and accurate references for verifying numerical solutions [22, 23]. The Navier method is recognised as a simple analytical approach suitable for structures with simply-supported boundary conditions [24]. Furthermore, the state space method has been utilised for FG beams [25]. The Ritz method is considered the most popular analytical method; therefore, it has attracted considerable interest from researchers. Karamanlı [26] examined the free vibration response of bi-directional FG beams based on the Ritz method using orthotropic polynomials. Nguyen et al. [27] employed the Ritz method based on polynomial functions and quasi-3D theory to analyse FG sandwich beams' buckling and free vibration. Şimşek and Shujairi [28] investigated FG sandwich beams' free and forced vibration using the Timoshenko beam theory and the Ritz method based on polynomial functions. Qin et al. [29] presented the vibration analysis of FG beams based on HSDT and Jacobi functions-Ritz solution. Balireddy et al. [30] utilised Rayleigh-Ritz's integral and the modal superposition method to analyse the buckling of bi-directional FG beams. Additionally, Dash et al. [31] researched the stability and vibration characteristics of variable stiffness laminated composite beams under thermo-mechanical loadings, employing a displacement-based Ritz approach to derive the matrix representation of the governing equations. Recently, Nguyen and his colleagues [32, 33] presented new Ritz-shape functions for the analysis of FG porous curved beams. Furthermore, the Ritz method has also been applied to the analysis of FG plates and shells [34–37].

Previous investigations into FG beams indicate that the application of Ritz solutions, particularly for static problems, has been relatively limited. Most studies have primarily employed Ritz solu-

tions for analysing vibration and stability, with no comprehensive research addressing the bending, buckling, and free vibration of FG beams [26–31]. Furthermore, existing studies often rely on approximation functions that may not inherently satisfy the essential boundary conditions of the problem [38–40]. To mitigate this issue, researchers have resorted to methodologies such as Lagrange multipliers [38, 39] or penalty functions [40]. However, these approaches increase the size of the stiffness and mass matrices, leading to heightened computational complexity and slower convergence rates [38–40].

This study introduces a Ritz method based on Laguerre polynomials to enhance computational efficiency and provide a comprehensive analysis, including bending, buckling, and free vibration, of FG beams with various boundary conditions. This approach ensures the satisfaction of essential boundary conditions, accelerates convergence, and reduces computational costs. Additionally, this research focuses on the analysis of FG beams, distinguishing it from the work of Nguyen et al. [33], which investigated bio-inspired helicoidal laminated composite beams. The authors will conduct an in-depth examination of the behaviour of FG beams, considering factors such as material distributions, boundary conditions, and slenderness ratios. The material properties of the FG beam are assumed to vary exponentially, and the equations of motion are derived using the Lagrange equations. Numerical examples are provided to validate the proposed method and to explore the influence of these parameters on the beam's displacement, frequency, critical buckling load, and stress.

## 2. Formulation

### *2.1. Functionally graded beam*

An analysis is conducted on an FG beam with a rectangular cross-section ($b \times h$) and a length $L$, composed of metal and ceramic materials (Fig. 1). The variation of material properties, including Young's modulus $E$, density $\rho$, and Poisson's ratio $\nu$, is assumed to occur continuously throughout the thickness of the beam. The effective material properties ($P$) of the FG beam are determined by applying the rule of mixture, allowing for the calculation of the beam's characteristics based on the varying material composition [38]:

$$P = P_m V_m + P_c V_c \tag{1}$$

where $P_m$ and $P_c$ denote the material properties of the metal and ceramic components, respectively. $V_m$ and $V_c$ represent the volume fractions of metal and ceramic within the FG beam. These volume fractions are assumed to be as follows [38]:

$$V_c(z) = \left(\frac{z}{h} + \frac{1}{2}\right)^k, \quad V_m(z) = 1 - V_c(z) \tag{2}$$

where $k$ represents the power-law index. Fig. 2 illustrates the variation of ceramic volume fraction ($V_c$) across the thickness of the FG beams. The observed trend indicates that an augmentation in the value of $k$ correlates with a reduction in $V_c$. In practice, various distribution laws exist for FG materials; however, the distribution form presented in Eq. (2) is often applied in real-world scenarios due to its simplicity and convenience in the manufacturing process [2, 38]. Under specific environmental conditions, alternative distribution laws may be employed to optimise the structure's performance [3].

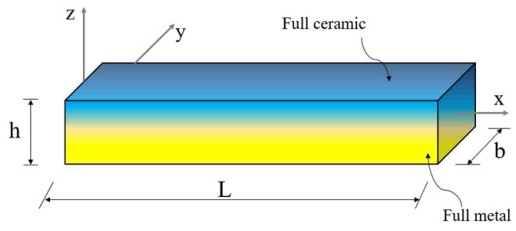


Figure 1. Geometry of FG beams

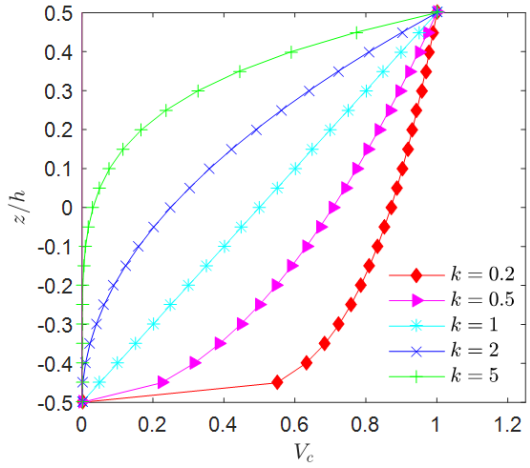


Figure 2. Variation of $V_c$ through the height of FG beams with various $k$

### 2.2. *Kinematics*

Based on the higher-order shear deformation theory, the displacement of FG beams is as follows [38]:

$$\mathbf{u} = \mathbf{z}\,\mathbf{w} \tag{3}$$

where $\mathbf{u} = \begin{bmatrix} u_1 & u_3 \end{bmatrix}^T$, $\mathbf{z} = \begin{bmatrix} 1 & -z & z - \dfrac{4z^3}{3h^2} & 0 \\ 0 & 0 & 0 & 1 \end{bmatrix}$, $\mathbf{w} = \begin{bmatrix} w_1 & w_{3,x} & \theta & w_3 \end{bmatrix}^T$, the comma notation indicates partial differentiation with respect to the coordinate subscript that follows. $u_1$ and $u_3$ represent the displacements of an arbitrary point in the $x$- and $z$-directions, while $w_1$ and $w_3$ denote the displacements of a point on the neutral axis in the $x$- and $z$-directions, respectively. Additionally, $\theta$ is the transverse shear strain of arbitrary point on the neutral axis presented by:

$$\theta = w_{3,x} - \gamma_0 \tag{4}$$

where $\gamma_0$ is the total bending rotation of the cross-sections at arbitrary point on the neutral axis [38].

The strain and displacement relationship of FG beams is elucidated as follows [38]:

$$\boldsymbol{\varepsilon} = \mathbf{H}\boldsymbol{\varepsilon}_0 \tag{5}$$

where $\boldsymbol{\varepsilon} = \begin{bmatrix} \varepsilon_{xx} & \gamma_{xz} \end{bmatrix}^T$, $\mathbf{H} = \begin{bmatrix} 1 & -z & z - \dfrac{4z^3}{3h^2} & 0 \\ 0 & 0 & 0 & 1 - \dfrac{4z^2}{h^2} \end{bmatrix}$, $\boldsymbol{\varepsilon}_0 = \begin{bmatrix} w_{1,x} & w_{3,xx} & \theta_{,x} & \theta \end{bmatrix}^T$.

The strain and stress relationship of the FG beam is expressed as [38]:

$$\boldsymbol{\sigma} = \mathbf{Q}\boldsymbol{\varepsilon} \tag{6}$$

where $\boldsymbol{\sigma} = \begin{bmatrix} \sigma_{xx} & \sigma_{xz} \end{bmatrix}^T$ and $\mathbf{Q} = \begin{bmatrix} E(z) & 0 \\ 0 & \dfrac{E(z)}{2[1+\nu(z)]} \end{bmatrix}$.

### 2.3. *Variational formulation*

The FG beam's strain energy ($\Pi_E$) is formulated as [38]:

$$\begin{aligned}\Pi_E &= \frac{1}{2}\int_V {}^T\sigma\varepsilon dV \\ &= \frac{1}{2}\int_0^L \Big[B_0(w_{1,x})^2 - 2B_1 w_{1,x}w_{3,xx} + B_2(w_{3,xx})^2 + 2B_3 w_{1,x}\theta_{,x} \\ &-2B_4 w_{3,xx}\theta_{,x} + B_5(\theta_{,x})^2 + B_6\theta^2\Big]dx\end{aligned} \tag{7}$$

where:

$$(B_0, B_1, B_2, B_3, B_4, B_5) = \int_{-h/2}^{h/2} E(z)\left[1, z, z^2, z - \frac{4z^3}{3h^2}, z\left(z - \frac{4z^3}{3h^2}\right), \left(z - \frac{4z^3}{3h^2}\right)^2\right] b\, dz \tag{8}$$

$$B_6 = \int_{-h/2}^{h/2} \frac{E(z)}{2(1+\nu)}\left(1 - \frac{4z^2}{h^2}\right)^2 b\, dz \tag{9}$$

The work done ($\Pi_V$) by the axial force $N_0$ and the uniform load $q$ is outlined as [23]:

$$\Pi_V = -\frac{1}{2}\int_0^L N_0 \left(w_{3,x}\right)^2 dx - \int_0^L q w_3\, dx \tag{10}$$

The kinetic energy ($\Pi_K$) is provided [38]:

$$\begin{aligned}\Pi_K &= \frac{1}{2}\int_V \rho(z)\dot{\mathbf{u}}^2\, dV \\ &= \frac{1}{2}\int_0^L \left[J_0\dot{w}_1^2 + J_0\dot{w}_3^2 - 2J_1\dot{w}_1\dot{w}_{3,x} + J_2\dot{w}_{3,x}^2 + 2J_3\dot{\theta}\dot{w}_1 - 2J_4\dot{\theta}\dot{w}_{3,x} + J_5\dot{\theta}^2\right]dx\end{aligned} \tag{11}$$

where the dot-superscript convention indicates differentiation with respect to time, and:

$$(J_0, J_1, J_2, J_3, J_4, J_5) = \int_{-h/2}^{h/2} \rho(z)\left[1, z, z^2, z - \frac{4z^3}{3h^2}, z\left(z - \frac{4z^3}{3h^2}\right), \left(z - \frac{4z^3}{3h^2}\right)^2\right] b\, dz \tag{12}$$

The total energy of the FG beams is expressed as [38]:

$$\Pi = \Pi_E + \Pi_V - \Pi_K \tag{13}$$

### 2.4. Ritz solution

Based on the Ritz solution, the displacement fields of the FG beam are delineated as follows [38]:

$$w_1(x,t) = \sum_{j=1}^{m} \Phi_{j,x}(x) w_{1j} e^{i\omega t}; \quad w_3(x,t) = \sum_{j=1}^{m} \Phi_j(x) w_{3j} e^{i\omega t}; \quad \theta(x,t) = \sum_{j=1}^{m} \Phi_{j,x}(x) \theta_j e^{i\omega t} \tag{14}$$

where $i = \sqrt{-1}$; $\omega$ represents the eigen-frequency, and the $w_{1j}$, $w_{3j}$ and $\theta_j$ are parameters that require determination. The Ritz-shape functions, denoted as $\Phi_j(x)$ and constructed upon Laguerre polynomials as detailed in Table 1, fulfill essential boundary conditions (BCs) for commonly encountered scenarios such as clamped-free (CF), simply-supported (SS), clamped-simply supported (CS), and clamped-clamped (CC) configurations [33]. This study focuses exclusively on the analysis of single-span beams. For multi-span beams, the Ritz method can also be applied to analyse their behaviour; this necessitates selecting appropriate shape functions and, at times, integrating the approach with the finite element method [41].

Substituting Eq. (14) into Eq. (13) and using Lagrange's equation [38]:

$$\frac{\partial \Pi}{\partial p_j} - \frac{d}{dt}\frac{\partial \Pi}{\partial \dot{p}_j} = 0 \tag{15}$$

with $p_j$ representing the values of $w_{1j}e^{i\omega t}$, $w_{3j}e^{i\omega t}$, and $\theta_j e^{i\omega t}$. The mechanical responses of the FG beams are achieved by solving:

$$\left(\mathbf{K} - N_0\mathbf{K_G} - \omega^2\mathbf{M}\right)\mathbf{d} = \mathbf{F} \tag{16}$$

where $\mathbf{K}$, $\mathbf{M}$, $\mathbf{K_G}$, $\mathbf{F}$, and $\mathbf{d}$ represent the stiffness matrix, mass matrix, geometry matrix, load vector, and column unknown vector, respectively, and additional details can be found in Appendix **B**.

Table 1. Shape functions and essential BCs of FG beams [33]

| BC | $\Phi_j(x)$ | $\Phi_{j,x}(x)$ | Essential BC |
|---|---|---|---|
| SS | $\left(\frac{x}{L}\right)\left(1-\frac{x}{L}\right)L_j\left(\frac{x}{L}\right)$ | $\left(\frac{x}{L}\right)\left(1-\frac{x}{L}\right)L_{j,x}\left(\frac{x}{L}\right) - \frac{2x}{L^2}L_j\left(\frac{x}{L}\right)$ | $\Phi_j(0)=0 \Rightarrow w_3(0)=0$;<br>$\Phi_j(L)=0 \Rightarrow w_3(L)=0$ |
| CF | $\left(\frac{x}{L}\right)^2 L_j\left(\frac{x}{L}\right)$ | $\left(\frac{x}{L}\right)^2 L_{j,x}\left(\frac{x}{L}\right) + \frac{2x}{L^2}L_j\left(\frac{x}{L}\right)$ | $\Phi_j(0)=0 \Rightarrow w_3(0)=0$;<br>$\Phi_{j,x}(0)=0 \Rightarrow w_1(0)=0$;<br>$w_{3,x}(0)=0, \theta(0)=0$ |
| CS | $\left(\frac{x}{L}\right)^2\left(1-\frac{x}{L}\right)L_j\left(\frac{x}{L}\right)$ | $\left(\frac{x}{L}\right)^2\left(1-\frac{x}{L}\right)L_{j,x}\left(\frac{x}{L}\right)$<br>$+\left(\frac{2x}{L^2}-\frac{3x^2}{L^3}\right)L_j\left(\frac{x}{L}\right)$ | $\Phi_j(0)=0 \Rightarrow w_3(0)=0$;<br>$\Phi_j(L)=0 \Rightarrow w_3(L)=0$;<br>$\Phi_{j,x}(0)=0 \Rightarrow w_1(0)=0$;<br>$w_{3,x}(0)=0, \theta(0)=0$ |
| CC | $\left(\frac{x}{L}\right)^2\left(1-\frac{x}{L}\right)^2 L_j\left(\frac{x}{L}\right)$ | $\left(\frac{x}{L}\right)^2\left(1-\frac{x}{L}\right)^2 L_{j,x}\left(\frac{x}{L}\right)$<br>$+2\left(\frac{x}{L^2}-\frac{3x^2}{L^3}+\frac{2x^3}{L^4}\right)L_j\left(\frac{x}{L}\right)$ | $\Phi_j(0)=0 \Rightarrow w_3(0)=0$;<br>$\Phi_j(L)=0 \Rightarrow w_3(L)=0$;<br>$\Phi_{j,x}(0)=0 \Rightarrow w_1(0)=0$;<br>$w_{3,x}(0)=0, \theta(0)=0$;<br>$\Phi_{j,x}(L)=0 \Rightarrow w_1(L)=0$;<br>$w_{3,x}(L)=0, \theta(L)=0$ |

Note: $L_j$ is Laguerre polynomial presented in Appendix **A**.

## 3. Results and discussion

This section presents numerical examples to assess the proposed solution and evaluate the influence of material properties, boundary conditions, and slenderness on the static, buckling, and vibration responses of FG beams. Two types of FG beams, namely $Al_2O_3$/Al and SiC/Al, comprising ceramic materials ($Al_2O_3$, SiC) and metal (Al) characteristics, as shown in Table 2, are considered. For simplicity, the values of normalised fundamental frequency (NFF), normalised critical buckling load (NCBL), normalised mid-span deflection (NMD), normalised axial stress (NAS), and normalised shear stress (NSS) are defined as follows [6, 12, 38, 39, 42]:

$$\bar{\omega} = \frac{\omega L^2}{h}\sqrt{\frac{\rho_m}{E_m}};\ \bar{N}_{cr} = \frac{N_0 L^2}{E_m b h^3};\ \bar{w} = \frac{100 w E_m b h^3}{q L^4};\ \bar{\sigma}_{xx} = \frac{bh}{qL}\sigma_{xx}(x,z);\ \bar{\sigma}_{xz} = \frac{bh}{qL}\sigma_{xz}(x,z) \quad (17)$$

Table 2. Material property

| No. | Description | $E$ (GPa) | $\rho$ (kg/m$^3$) | $\nu$ |
|---|---|---|---|---|
| Ceramic | $Al_2O_3$ | 380 | 3960 | 0.3 |
| | SiC | 427 | 3100 | 0.17 |
| Metal | Al | 70 | 2702 | 0.3 |

### *3.1. Convergence investigation*

To evaluate the convergence of the present method, an analysis is conducted on $Al_2O_3$/Al and SiC/Al FG beams ($k = 1$, $L/h = 20$) under various boundary conditions. The results of the investigation are presented in Table 3, which includes the NFF, NCBL, and NMD of FG beams with respect to the parameter $m$. It is evident from the data that the boundary conditions influence the convergence of the method. Specifically, the results demonstrate convergence at $m = 5$ for SS beams, $m = 9$ for CF, CS, and CC beams. Consequently, these specific points are utilised for subsequent analyses. Comparatively, the current method exhibits faster convergence in contrast to Şimşek [38] ($m = 14$), Nguyen et al. [39] ($m = 14$), and Mantari and Canales [40] ($m = 12$ for buckling and $m = 80$ for vibration behaviour), providing compelling evidence for the efficiency of the present method.

Table 3. Convergence studies for FG beams

| BC | $m$ | | | | | |
|---|---|---|---|---|---|---|
| | 1 | 3 | 5 | 7 | 9 | 11 |
| $Al_2O_3$/Al | | | | | | |
| 1. Normalised fundamental frequency (NFF) | | | | | | |
| SS | 8.681 | 4.206 | 4.205 | 4.205 | 4.205 | 4.205 |
| CF | 8.681 | 1.513 | 1.501 | 1.501 | 1.501 | 1.501 |
| CS | 9.481 | 6.556 | 6.546 | 6.545 | 6.545 | 6.545 |
| CC | 11.844 | 9.440 | 9.435 | 9.433 | 9.432 | 9.432 |
| 2. Normalised critical buckling load (NCBL) | | | | | | |
| SS | 79.864 | 26.577 | 26.562 | 26.562 | 26.562 | 26.562 |
| CF | 79.864 | 6.711 | 6.667 | 6.667 | 6.667 | 6.667 |
| CS | 111.092 | 54.246 | 54.036 | 54.036 | 54.036 | 54.036 |
| CC | 141.923 | 104.648 | 104.564 | 104.563 | 104.563 | 104.563 |

| BC | *m* | | | | | |
|---|---|---|---|---|---|---|
| | 1 | 3 | 5 | 7 | 9 | 11 |
| 3. Normalised mid-span deflection (NMD) | | | | | | |
| SS | 1.174 | 5.805 | 5.805 | 5.805 | 5.805 | 5.805 |
| CF | 1.174 | 19.417 | 19.717 | 19.721 | 19.722 | 19.723 |
| CS | 1.181 | 2.331 | 2.339 | 2.340 | 2.340 | 2.340 |
| CC | 0.694 | 1.182 | 1.184 | 1.184 | 1.185 | 1.184 |
| SiC/Al | | | | | | |
| 1. Normalised fundamental frequency (NFF) | | | | | | |
| SS | 9.700 | 4.698 | 4.697 | 4.697 | 4.697 | 4.697 |
| CF | 9.700 | 1.690 | 1.677 | 1.677 | 1.677 | 1.677 |
| CS | 10.596 | 7.325 | 7.313 | 7.312 | 7.312 | 7.312 |
| CC | 13.240 | 10.551 | 10.546 | 10.544 | 10.543 | 10.542 |
| 2. Normalised critical buckling load (NCBL) | | | | | | |
| SS | 86.859 | 28.883 | 28.866 | 28.866 | 28.866 | 28.866 |
| CF | 86.859 | 7.291 | 7.244 | 7.244 | 7.244 | 7.244 |
| CS | 120.876 | 58.976 | 58.747 | 58.746 | 58.746 | 58.746 |
| CC | 154.490 | 113.854 | 113.762 | 113.762 | 113.762 | 113.762 |
| 3. Normalised mid-span deflection (NMD) | | | | | | |
| SS | 1.079 | 5.342 | 5.342 | 5.342 | 5.342 | 5.342 |
| CF | 1.079 | 17.869 | 18.145 | 18.148 | 18.149 | 18.150 |
| CS | 1.086 | 2.144 | 2.151 | 2.152 | 2.152 | 2.152 |
| CC | 0.637 | 1.086 | 1.088 | 1.088 | 1.089 | 1.088 |

### *3.2. Buckling and free vibration responses*

Tables 4 and 5 display the NFF and NCBL of FG beams across various $L/h$ ratios, $k$, and BCs. A comparative analysis is drawn between the current findings and the outcomes derived by Şimşek [38] utilising the Ritz method based on polynomial functions, as well as investigations by Benzid and Tati [12], and Vo et al. [6] utilising FEM. The congruence between the present results and the existing literature (Refs. [6, 12, 38]) validates the accuracy and reliability of the proposed methodology. Furthermore, it is observed that the NFF and NCBL values for SiC/Al beams surpass those of $Al_2O_3$/Al beams, attributed to the higher modulus of elasticity of SiC compared to $Al_2O_3$, coupled with the smaller mass density of SiC. Fig. 3 illustrates the NFF and NCBL trends of SiC/Al beams ($L/h = 10$) under varying $k$ and BCs. The analysis reveals that an increase in $k$ corresponds to a decrease in NFF and NCBL, indicating the beam's increased flexibility. This trend corroborates with established principles in the context of mechanical vibrations and structural buckling behaviours, wherein a decreased structural stiffness results in reduced vibration frequencies and buckling loads. Additionally, the graphical representation depicts that the CC beams exhibit the highest NFF and NCBL values, followed by a gradual decline in results for CS, SS, and CF beams. This emphasises the significant impact of boundary conditions on the free vibration and buckling characteristics of FG beams.

Fig. 4 illustrates the variations in the NFF and NCBL of SiC/Al beams ($k = 1$) with respect to the $L/h$ ratio. The analysis reveals a distinct trend among different boundary conditions: CC and CS beams exhibit a significant rise in results for $L/h$ ratios below 15, while showing a more modest increase for $L/h$ ratios exceeding 15. In contrast, SS and CF beams demonstrate slight incremental

Table 4. NFF of FG beams

| BC | $L/h$ | Reference | $k$ | | | | |
|---|---|---|---|---|---|---|---|
| | | | 0 | 0.5 | 2 | 5 | 10 |
| $Al_2O_3$/Al | | | | | | | |
| SS | 5 | Present | 5.1527 | 4.4107 | 3.6264 | 3.4012 | 3.2816 |
| | | Nguyen et al. [39] | 5.1528 | 4.4102 | 3.6264 | 3.4009 | 3.2815 |
| | 20 | Present | 5.4603 | 4.6511 | 3.8361 | 3.6485 | 3.5390 |
| | | Şimşek [38] | 5.4603 | 4.6516 | 3.8361 | 3.6485 | 3.5390 |
| CF | 5 | Present | 1.8954 | 1.6181 | 1.3326 | 1.2593 | 1.2184 |
| | | Şimşek [38] | 1.8952 | 1.6182 | 1.3325 | 1.2592 | 1.2183 |
| | 20 | Present | 1.9496 | 1.6603 | 1.3696 | 1.3034 | 1.2645 |
| | | Şimşek [38] | 1.9495 | 1.6605 | 1.3696 | 1.3033 | 1.2645 |
| CS | 5 | Present | 7.6042 | 6.5477 | 5.3779 | 4.9686 | 4.7613 |
| | 20 | Present | 8.4930 | 7.2380 | 5.9690 | 5.6692 | 5.4956 |
| CC | 5 | Present | 10.0714 | 8.7468 | 7.1773 | 6.4940 | 6.1656 |
| | | Şimşek [38] | 10.0699 | 8.7463 | 7.1766 | 6.4940 | 6.1652 |
| | 20 | Present | 12.2247 | 10.4284 | 8.5980 | 8.1452 | 7.8864 |
| | | Şimşek [38] | 12.2238 | 10.4287 | 8.5975 | 8.1448 | 7.8860 |
| SiC/Al | | | | | | | |
| SS | 5 | Present | 6.2008 | 5.0786 | 3.9219 | 3.5596 | 3.3901 |
| | 20 | Present | 6.5440 | 5.3430 | 4.1440 | 3.8183 | 3.6611 |
| CF | 5 | Present | 2.2758 | 1.8608 | 1.4403 | 1.3179 | 1.2596 |
| | 20 | Present | 2.3361 | 1.9071 | 1.4794 | 1.3640 | 1.3082 |
| CS | 5 | Present | 9.1946 | 7.5649 | 5.8320 | 5.2058 | 4.9140 |
| | 20 | Present | 10.1828 | 8.3170 | 6.4494 | 5.9335 | 5.6846 |
| CC | 5 | Present | 12.2611 | 10.1572 | 7.8165 | 6.8153 | 6.3560 |
| | 20 | Present | 14.6685 | 11.9894 | 9.2941 | 8.5265 | 8.1561 |

Table 5. NCBL of FG beams

| BC | $L/h$ | Reference | $k$ | | | | |
|---|---|---|---|---|---|---|---|
| | | | 0 | 0.5 | 2 | 5 | 10 |
| $Al_2O_3$/Al | | | | | | | |
| SS | 5 | Present | 48.5959 | 31.8663 | 19.0709 | 15.6435 | 14.0512 |
| | | Benzid and Tati [12] | 48.6000 | – | 19.0286 | 15.5437 | 13.9335 |
| | | Vo et al. [6] | 48.8401 | 32.0094 | 19.1605 | 15.7400 | 14.1468 |
| | 10 | Present | 52.2378 | 33.9673 | 20.3662 | 17.0817 | 15.4993 |
| | | Benzid and Tati [12] | 52.2857 | – | 20.3633 | 17.0589 | 15.4690 |
| | | Vo et al. [6] | 52.3082 | 34.0087 | 20.3936 | 17.1118 | 15.5291 |
| CF | 5 | Present | 13.0594 | 8.4918 | 5.0916 | 4.2704 | 3.8748 |
| | | Benzid and Tati [12] | 13.0714 | – | 5.0786 | 4.2634 | 3.8662 |
| | | Vo et al. [6] | 13.0771 | 8.5020 | 5.0979 | 4.2776 | 3.8821 |

| BC | $L/h$ | Reference | $k$ | | | | |
|---|---|---|---|---|---|---|---|
| | | | 0 | 0.5 | 2 | 5 | 10 |
| | 10 | Present | 13.3091 | 8.6343 | 5.1796 | 4.3711 | 3.9775 |
| | | Benzid and Tati [12] | 13.3714 | – | 5.1816 | 4.3709 | 3.9765 |
| | | Vo et al. [6] | 13.3742 | 8.6714 | 5.2027 | 4.3976 | 4.0046 |
| CS | 5 | Present | 90.6246 | 60.0244 | 35.8438 | 28.6499 | 25.4414 |
| | 10 | Present | 104.1431 | 67.9265 | 40.6999 | 33.8588 | 30.6072 |
| CC | 5 | Present | 152.1473 | 102.2704 | 60.8783 | 46.8870 | 40.9884 |
| | | Benzid and Tati [12] | 151.9500 | – | 60.3000 | 45.9138 | 39.9214 |
| | | Vo et al. [6] | 154.5500 | 103.7490 | 61.7925 | 47.7562 | 41.8042 |
| | 10 | Present | 194.3835 | 127.4653 | 76.2838 | 62.5740 | 56.2047 |
| | | Benzid and Tati [12] | 194.4000 | – | 76.1218 | 62.1955 | 55.7505 |
| | | Vo et al. [6] | 195.3610 | 128.0500 | 76.6677 | 62.9786 | 56.5971 |
| SiC/Al | | | | | | | |
| SS | 5 | Present | 55.1184 | 35.4591 | 20.3134 | 16.3233 | 14.5909 |
| | 10 | Present | 58.8459 | 37.6173 | 21.6100 | 17.7978 | 16.1207 |
| CF | 5 | Present | 14.7115 | 9.4043 | 5.4025 | 4.4494 | 4.0302 |
| | 10 | Present | 14.9648 | 9.5498 | 5.4902 | 4.5524 | 4.1388 |
| CS | 5 | Present | 103.6240 | 67.1765 | 38.3551 | 29.9452 | 26.3716 |
| | 10 | Present | 117.6099 | 75.3559 | 43.2458 | 35.2973 | 31.8151 |
| CC | 5 | Present | 176.0497 | 115.4464 | 65.5919 | 49.1226 | 42.3857 |
| | 10 | Present | 220.4735 | 141.8362 | 81.2536 | 65.2930 | 58.3638 |

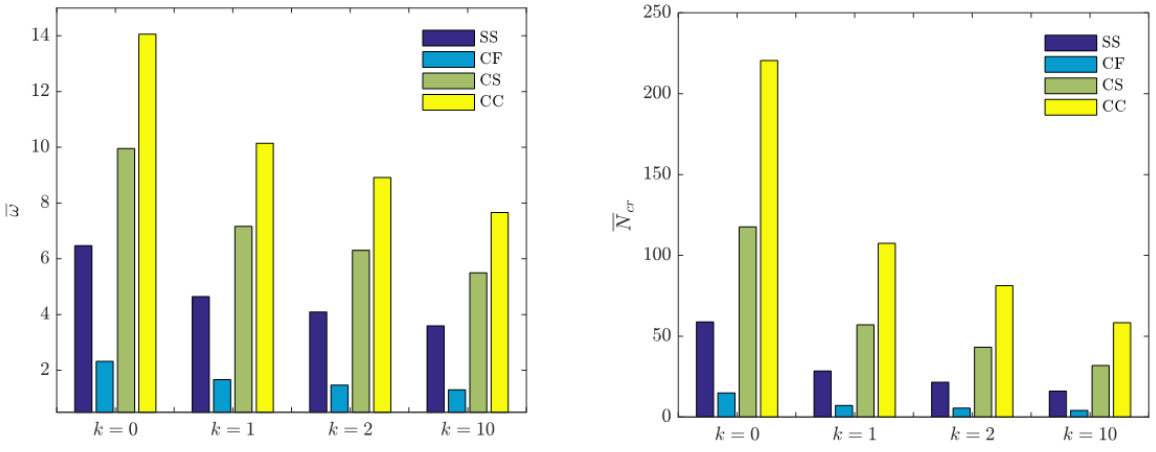


(a) NFF (b) NCBL

Figure 3. NFF and NCBL of SiC/Al beams with various $k$ and BCs ($L/h = 10$)

changes across all $L/h$ ratios. Moreover, the impact of the $L/h$ ratio increase on NFF and NCBL is most pronounced in CC beams and least pronounced in CF beams. For example, the percentage difference in NFF between $L/h = 5$ and $L/h = 15$ is 16.5%, 9.2%, 4.9%, and 2.3% for CC, CS, SS, and CF beams, respectively. Additionally, the disparity in NCBL between $L/h = 5$ and $L/h = 15$ is 27.4%, 14.3%, 7.1%, and 1.8% for CC, CS, SS, and CF beams, underscoring the varying sensitivities of different beam types to changes in the $L/h$ ratio.

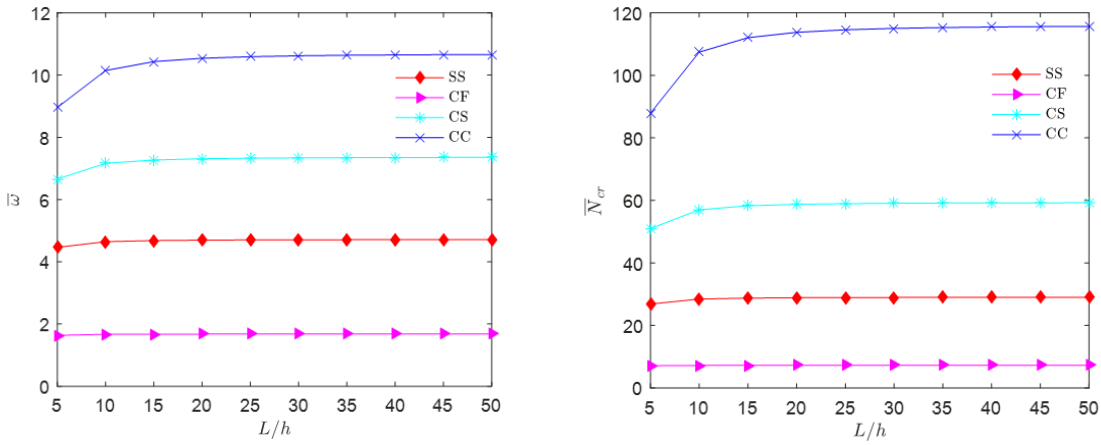


(a) NFF (b) NCBL

Figure 4. NFF and NCBL of SiC/Al beams with respect to $L/h$ ratios ($k = 1$)

Table 6 and Fig. 5 present the influence of axial force on the NFF of FG beams ($L/h = 20$). The impact of axial force on the NFF is significant across all values of $k$ and BCs. Notably, the NFF decreases as the axial force transitions from tension to compression, reaching zero values at the critical buckling load. This observation suggests that tensile forces induce a stiffening effect, whereas compressive forces induce a softening effect on the FG beams.

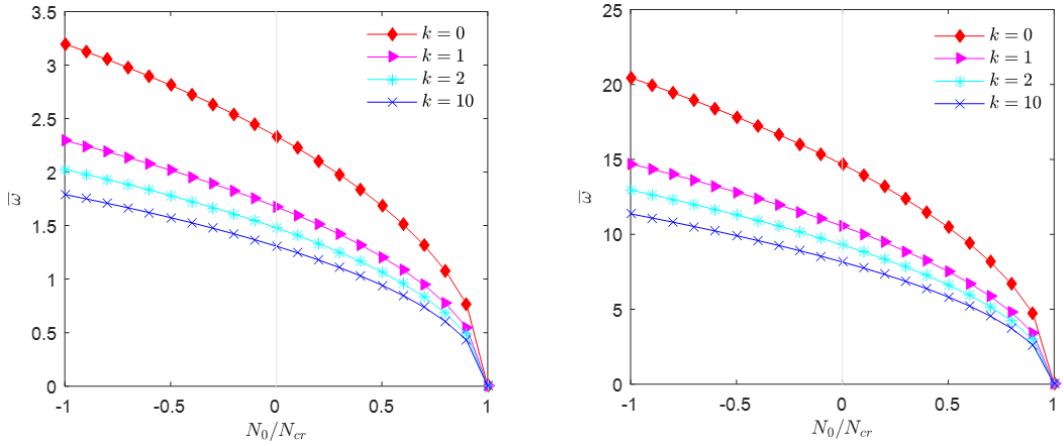


(a) CF beam (b) CC beam

Figure 5. Effect of axial force on NFF of SiC/Al beams ($L/h = 20$)

Furthermore, Fig. 6 showcases the first vibration mode shapes of SiC/Al beams ($k = 2$) with various $L/h$ ratios and BCs. It is evident that for $L/h = 3$, the predominant mode shapes for CC, CS, and SS beams are of the shear type, whereas CF beams exhibit a bending mode shape. Meanwhile, at $L/h = 6$, the mode shapes for CS, SS, and CF beams are bending mode shapes, and CC beams display shear mode shapes. At $L/h = 30$, all BCs demonstrate bending mode shapes. This observation indicates that the shear effect is contingent on the $L/h$ ratio and the specific BCs. Additionally, the significance of the shear effect is notably pronounced in CC beams with smaller $L/h$ ratios ($L/h = 3, 6$), whereas it is not as prominent in CF beams. In addition, upon closer examination of the CF

Table 6. Effect of the axial force on NFF of FG beams ($L/h = 20$)

| BC | $k$ | $N_{cr}$ | $N_0 = -0.8N_{cr}$ (Tension) | $N_0 = -0.4N_{cr}$ (Tension) | $N_0 = 0.4N_{cr}$ (Compression) | $N_0 = 0.8N_{cr}$ (Compression) |
|---|---|---|---|---|---|---|
| $Al_2O_3$/Al | | | | | | |
| SS | 0 | 53.2364 | 7.3258 | 6.4607 | 4.2295 | 2.4419 |
| | 1 | 26.5619 | 5.6417 | 4.9755 | 3.2572 | 1.8806 |
| | 5 | 17.4842 | 4.8950 | 4.3169 | 2.8261 | 1.6317 |
| | 10 | 15.9099 | 4.7481 | 4.1874 | 2.7413 | 1.5827 |
| CF | 0 | 13.3730 | 2.5468 | 2.2748 | 1.5336 | 0.9007 |
| | 1 | 6.6673 | 1.9610 | 1.7515 | 1.1807 | 0.6934 |
| | 5 | 4.3970 | 1.7025 | 1.5207 | 1.0253 | 0.6022 |
| | 10 | 4.0040 | 1.6517 | 1.4753 | 0.9948 | 0.5843 |
| CS | 0 | 108.1872 | 11.3034 | 10.0056 | 6.6124 | 3.8417 |
| | 1 | 54.0356 | 8.7112 | 7.7107 | 5.0954 | 2.9601 |
| | 5 | 35.4769 | 7.5445 | 6.6785 | 4.4142 | 2.5647 |
| | 10 | 32.2498 | 7.3130 | 6.4738 | 4.2792 | 2.4864 |
| CC | 0 | 208.9512 | 16.2122 | 14.3747 | 9.5389 | 5.5561 |
| | 1 | 104.5634 | 12.5113 | 11.0923 | 7.3589 | 4.2855 |
| | 5 | 68.3268 | 10.7991 | 9.5764 | 6.3569 | 3.7036 |
| | 10 | 61.9973 | 10.4541 | 9.2711 | 6.1557 | 3.5870 |
| SiC/Al | | | | | | |
| SS | 0 | 59.8590 | 8.7797 | 7.7430 | 5.0690 | 2.9266 |
| | 1 | 28.8663 | 6.3017 | 5.5576 | 3.6383 | 2.1006 |
| | 5 | 18.2097 | 5.1228 | 4.5179 | 2.9576 | 1.7076 |
| | 10 | 16.5554 | 4.9119 | 4.3319 | 2.8359 | 1.6373 |
| CF | 0 | 15.0295 | 3.0518 | 2.7258 | 1.8376 | 1.0792 |
| | 1 | 7.2437 | 2.1903 | 1.9563 | 1.3188 | 0.7745 |
| | 5 | 4.5789 | 1.7817 | 1.5915 | 1.0730 | 0.6302 |
| | 10 | 4.1669 | 1.7087 | 1.5263 | 1.0292 | 0.6045 |
| CS | 0 | 121.7259 | 13.5530 | 11.9967 | 7.9279 | 4.6057 |
| | 1 | 58.7465 | 9.7329 | 8.6150 | 5.6927 | 3.3071 |
| | 5 | 36.9542 | 7.8964 | 6.9900 | 4.6199 | 2.6843 |
| | 10 | 33.5527 | 7.5644 | 6.6964 | 4.4264 | 2.5720 |
| CC | 0 | 235.3837 | 19.4555 | 17.2495 | 11.4448 | 6.6654 |
| | 1 | 113.7619 | 13.9859 | 12.3992 | 8.2251 | 4.7896 |
| | 5 | 71.1910 | 11.3050 | 10.0248 | 6.6543 | 3.8768 |
| | 10 | 64.4828 | 10.8113 | 9.5880 | 6.3663 | 3.7098 |

beam (Fig. 6(d)), the mode shape $\theta$ is equal to 0 at the clamped end ($x = 0$) and nearly zero at the free end ($x = L$). Physically, $\theta$ represents the transverse shear strain at any point on the neutral axis, as described in Eq. (4). It can be observed that at $x = 0$, the clamped connection necessitates $\theta = 0$, while at $x = L$, the curvature of the beam approximates the total bending rotation of the cross-sections, thus resulting in $\theta \approx 0$.

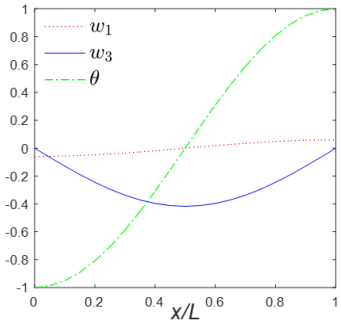


(a) SS beam ($L/h = 3$)

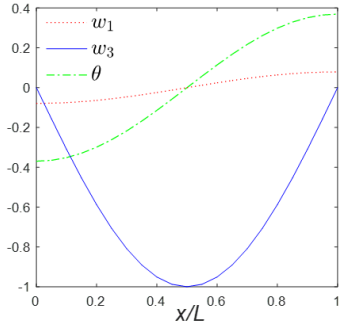


(b) SS beam ($L/h = 6$)

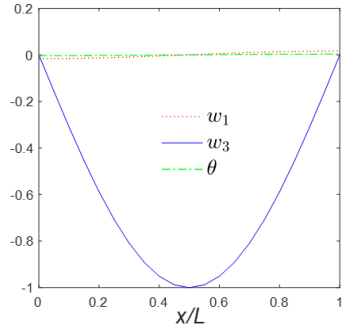


(c) SS beam ($L/h = 30$)

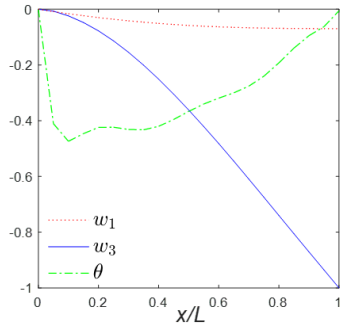


(d) CF beam ($L/h = 3$)

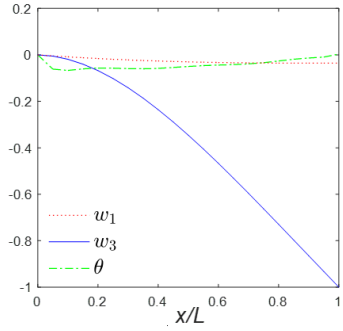


(e) CF beam ($L/h = 6$)

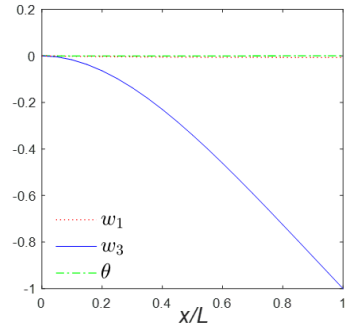


(f) CF beam ($L/h = 30$)

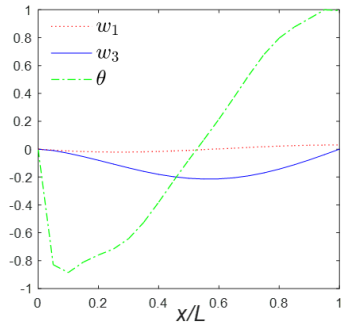


(g) CS beam ($L/h = 3$)

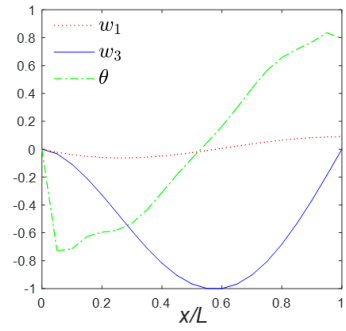


(h) CS beam ($L/h = 6$)

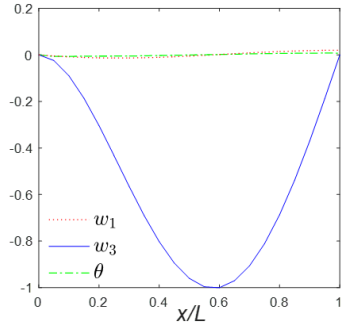


(i) CS beam ($L/h = 30$)

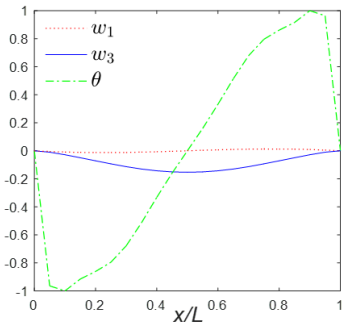


(j) CC beam ($L/h = 3$)

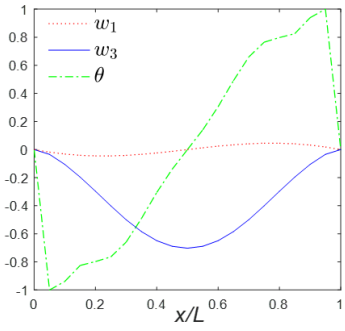


(k) CC beam ($L/h = 6$)

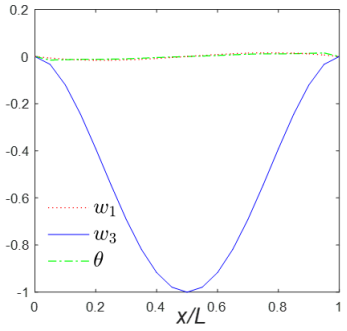


(l) CC beam ($L/h = 30$)

Figure 6. First vibration mode shape of SiC/Al beams with various BCs ($k = 2$)

### 3.3. Bending response

Tables 7 and 8 depict the NMD, NAS, and NSS of FG beams across different BCs, $L/h$ ratios, and $k$. A comparative analysis is conducted with the findings of Benzid and Tati [12] and Vo et al. [6], who employed FEM, and Li et al. [23] using an analytical method. The results demonstrate complete accordance with the references above (Refs. [6, 12, 23]), providing robust evidence for the accuracy of the proposed approach in addressing bending problems. Additionally, the outcomes for SiC/Al beams are smaller than those of $Al_2O_3$/Al beams, aligning with theoretical expectations.

Table 7. NMD of FG beams

| BC | $L/h$ | Reference | $k$ | | | |
|---|---|---|---|---|---|---|
| | | | 0 | 2 | 5 | 10 |
| $Al_2O_3$/Al | | | | | | |
| SS | 5 | Present | 3.1654 | 8.0677 | 9.8281 | 10.9381 |
| | | Benzid and Tati [12] | 3.1652 | 8.0878 | 9.8893 | 11.0278 |
| | 20 | Present | 2.8962 | 7.4421 | 8.8182 | 9.6905 |
| | | Benzid and Tati [12] | 2.8903 | 7.4270 | 8.8081 | 9.6826 |
| CF* | 5 | Present | 28.7504 | 73.6411 | 88.1942 | 97.4011 |
| | | Vo et al. [6] | 28.7555 | 73.6482 | 88.2044 | 97.4151 |
| | 20 | Present | 27.7020 | 71.2067 | 84.2720 | 92.5560 |
| | | Vo et al. [6] | 27.7029 | 71.2051 | 84.2712 | 92.5571 |
| CS | 5 | Present | 1.4298 | 3.6068 | 4.5421 | 5.1299 |
| | 20 | Present | 1.1689 | 3.0009 | 3.5662 | 3.9242 |
| CC | 5 | Present | 0.8503 | 2.1162 | 2.7713 | 3.1826 |
| | | Benzid and Tati [12] | 0.8629 | 2.1684 | 2.8894 | 3.3428 |
| | | Vo et al. [6] | 0.8501 | 2.1151 | 2.7700 | 3.1812 |
| | 20 | Present | 0.5934 | 1.5213 | 1.8166 | 2.0036 |
| | | Benzid and Tati [12] | 0.5924 | 1.5198 | 1.8185 | 2.0075 |
| | | Vo et al. [6] | 0.5933 | 1.5203 | 1.8155 | 2.0027 |
| SiC/Al | | | | | | |
| SS | 5 | Present | 2.7914 | 7.5752 | 9.4192 | 10.5330 |
| | 20 | Present | 2.5759 | 7.0211 | 8.4669 | 9.3127 |
| CF* | 5 | Present | 25.4869 | 69.3492 | 84.6199 | 93.6768 |
| | 20 | Present | 24.6466 | 67.1925 | 80.9216 | 88.9390 |
| CS | 5 | Present | 1.2481 | 3.3673 | 4.3449 | 4.9525 |
| | 20 | Present | 1.0387 | 2.8299 | 3.4236 | 3.7722 |
| CC | 5 | Present | 0.7328 | 1.9611 | 2.6444 | 3.0802 |
| | 20 | Present | 0.5264 | 1.4330 | 1.7428 | 1.9259 |

Note: *The deflection of CF beams at $x = L$.

Furthermore, Fig. 7 presents the displacement distribution ($w_3$) along the length of SS and CS SiC/Al beams with various $k$. The analysis reveals an anticipated increase in NMD with a corresponding rise in $k$. This aligns with theoretical expectations regarding the influence of material gradient on the structural response.

Table 8. NAS and NSS of SS FG beams

| Stress | $L/h$ | Reference | $k$ | | | |
|---|---|---|---|---|---|---|
| | | | 0 | 2 | 5 | 10 |
| $Al_2O_3/Al$ | | | | | | |
| $\bar{\sigma}_{xx}$ | 5 | Present | 3.8020 | 6.8827 | 8.1107 | 9.7123 |
| | | Benzid and Tati [12] | 3.7494 | 6.7665 | 7.9418 | 9.5217 |
| | | Vo et al. [6] | 3.8040 | 6.8860 | 8.1150 | 9.7170 |
| | | Li et al. [23] | 3.8020 | 6.8812 | 8.1030 | 9.7063 |
| | 20 | Present | 15.0130 | 27.0992 | 31.8132 | 38.1388 |
| | | Benzid and Tati [12] | 14.9689 | 27.0103 | 31.7204 | 38.0376 |
| | | Vo et al. [6] | 15.0200 | 27.1100 | 31.8300 | 38.1600 |
| | | Li et al. [23] | 15.0130 | 27.0989 | 31.8112 | 38.1372 |
| $\bar{\sigma}_{xz}$ | 5 | Present | 0.7333 | 0.6707 | 0.5906 | 0.6467 |
| | | Benzid and Tati [12] | 0.7470 | 0.6948 | 0.6211 | 0.6837 |
| | | Vo et al. [6] | 0.7335 | 0.6700 | 0.5907 | 0.6477 |
| | | Li et al. [23] | 0.7500 | 0.6787 | 0.5790 | 0.6436 |
| | 20 | Present | 0.7466 | 0.6837 | 0.6032 | 0.6607 |
| | | Benzid and Tati [12] | 0.7470 | 0.6948 | 0.6212 | 0.6837 |
| | | Vo et al. [6] | 0.7470 | 0.6777 | 0.6039 | 0.6682 |
| | | Li et al. [23] | 0.7500 | 0.6787 | 0.5790 | 0.6436 |
| SiC/Al | | | | | | |
| $\bar{\sigma}_{xx}$ | 5 | Present | 3.7968 | 7.1202 | 8.4414 | 10.1516 |
| | 20 | Present | 15.0117 | 28.0519 | 33.1042 | 39.8392 |
| $\bar{\sigma}_{xz}$ | 5 | Present | 0.7342 | 0.6590 | 0.5702 | 0.6343 |
| | 20 | Present | 0.7468 | 0.6722 | 0.5824 | 0.6482 |

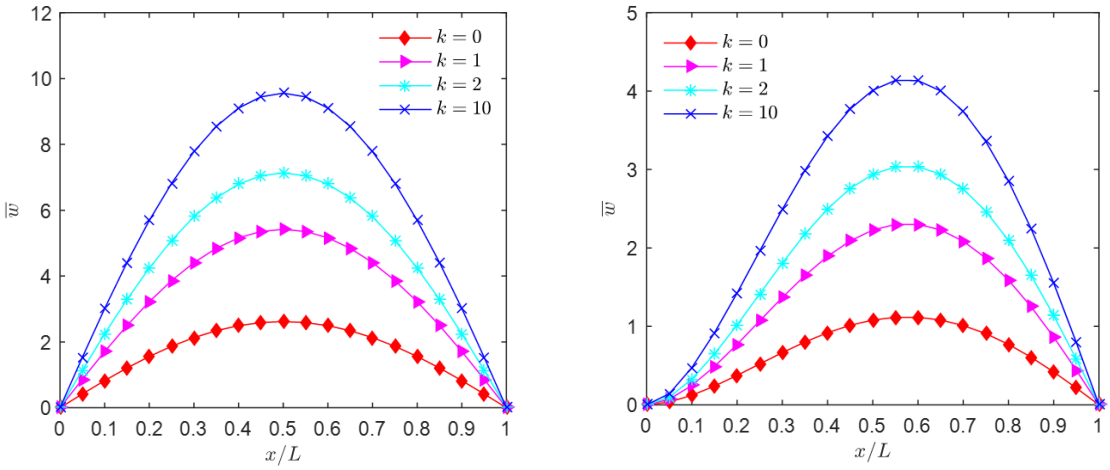


(a) SS beam (b) CS beam

Figure 7. Deflection of SiC/Al beams with various BCs ($L/h$ = 10)

Fig. 8 displays the NAS and NSS profiles of SS SiC/Al beams across the thickness of the beams. The analysis reveals a significant influence of the $k$ on the NAS and NSS characteristics of the beams. Specifically, when $k = 0$, the FG beams exhibit behaviour akin to ceramic beams, resulting in a linear variation of NAS throughout the beam thickness, with a vanishing effect at the mid-plane. Meanwhile, the NSS demonstrates a non-linear and symmetric distribution through the mid-plane. Conversely, as the $k$ index increases, the FG beam's neutral plane shifts toward the beam's top surface. In addition, the NSS vanished at the top and bottom surfaces of the beam, as expected. In Fig. 9, the NAS and NSS profiles of SS SiC/Al beams along the length of the beams are depicted. These profiles illustrate that the NAS reaches its peak while the NSS diminishes to zero at the mid-span.

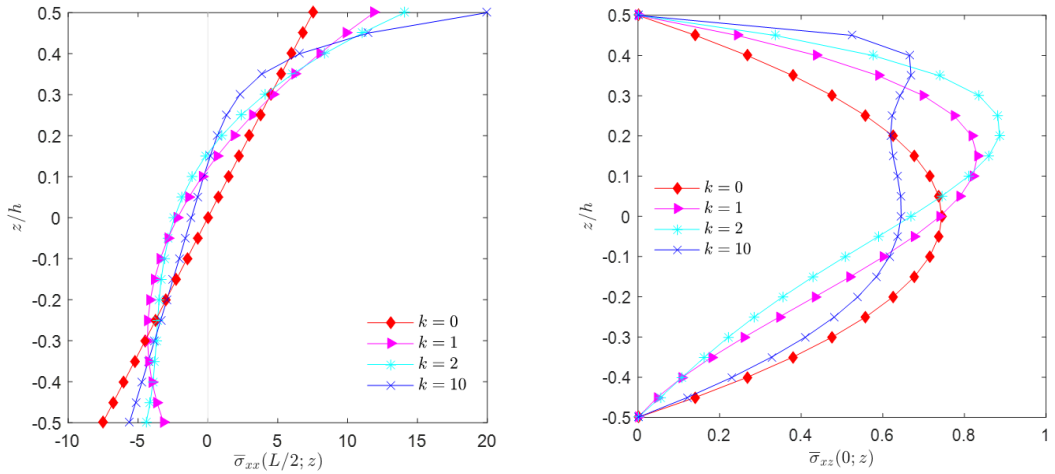


(a) NAS (b) NSS

Figure 8. NAS and NSS of SiC/Al beams with various $k$ ($L/h = 10$)

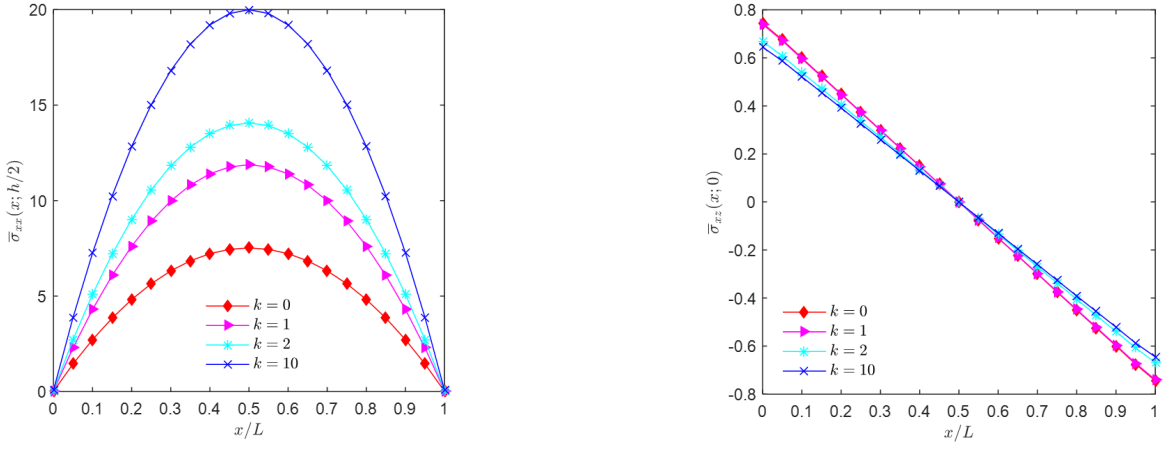


(a) NAS (b) NSS

Figure 9. NAS and NSS of SiC/Al beams with various $k$ ($L/h = 10$)

Fig. 10 showcases the NMD of SiC/Al beams ($k = 1$) with respect to the $L/h$ ratio. It is evident that as the $L/h$ ratio increases, the results noticeably decrease for $L/h < 15$ and exhibit a slight increase for $L/h \geq 15$ across all beams. Moreover, the decline in NMD due to the increase in $L/h$ ratio is most pronounced for CC beams, while being least noticeable for CF beams. For example, the

percentage difference in NMD between $L/h = 5$ and $L/h = 15$ amounts to 24.1%, 14.2%, 6.4%, and 5.4% for CC, CS, SS, and CF beams, respectively. Furthermore, it is observed that the NMD is at its minimum for CC beams and at its maximum for CF beams.

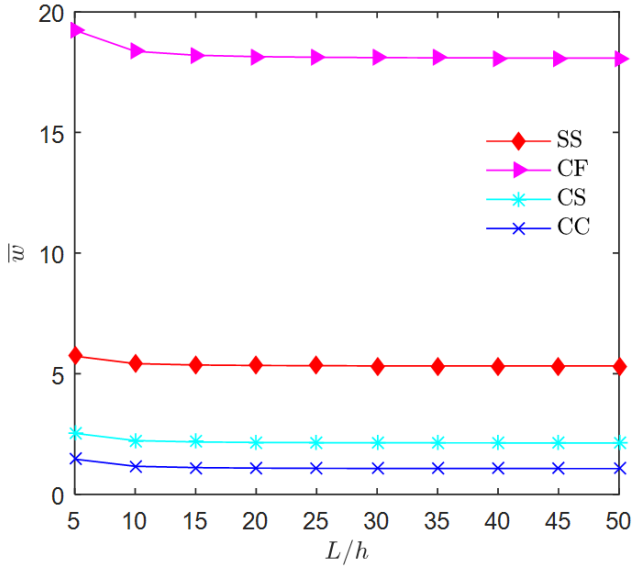


Figure 10. NMD of SiC/Al beams with respect to $L/h$ ratio ($k = 1$)

## 4. Conclusions

This paper presents a novel analytical approach for investigating FG beams' bending, buckling, and free vibration characteristics. Specifically, two types of FG beams, namely $Al_2O_3$/Al and SiC/Al, are examined within the study. The material gradient within the beams follows a power-law distribution. The beam displacement uses a higher-order shear deformation theory, while the governing equations are derived from Lagrange equations. Numerical illustrations within the study demonstrate the reliability and effectiveness of the proposed methodologies, exploring the influence of the power-law index, boundary condition, and slenderness on the mechanical behaviours of FG beams. Several key observations emerge from the study:

- The straight form of Laguerre polynomials proves to be notably efficient for the comprehensive analysis of FG beams.

- The NFF and NCBL are maximised for CC beams, while they are minimised for CF beams. Conversely, the NMD is minimised for CC beams and maximised for CF beams.

- The power-law index exerts a pronounced influence on the mechanical response of FG beams.

- The NFF and NCBL values for SiC/Al beams surpass those of $Al_2O_3$/Al beams, while the NMD for SiC/Al beams is observed to be inferior to that of $Al_2O_3$/Al beams.

- These findings contribute to the scientific community and offer significant insights for designers aiming to develop engineering systems prioritising safety and cost-effectiveness.

## Acknowledgements

This research is funded by Vietnam National Foundation for Science and Technology Development (NAFOSTED) under grant number 107.02-2023.57.

## References


[1] Koizumi, M. (1997). FGM activities in Japan. *Composites Part B: Engineering*, 28(1-2):1–4.

[2] Saleh, B., Jiang, J., Fathi, R., Al-hababi, T., Xu, Q., Wang, L., Song, D., Ma, A. (2020). 30 Years of functionally graded materials: An overview of manufacturing methods, Applications and Future Challenges. *Composites Part B: Engineering*, 201:108376.

[3] Ghatage, P. S., Kar, V. R., Sudhagar, P. E. (2020). On the numerical modelling and analysis of multi-directional functionally graded composite structures: A review. *Composite Structures*, 236:111837.

[4] Do, D. T. T., Thai, S. (2025). A catboost-based surrogate model for fast prediction of free vibration response in tri-directional functionally graded plates. *Journal of Science and Technology in Civil Engineering (JSTCE) - HUCE*, 19(4):58–68.

[5] Chau-Dinh, T., La-Tuan, M., Le-Phuong, B. (2025). A CS-MITC3+ plate element for static analysis of HSDT-type functionally graded plates under thermo-mechanical loading. *Journal of Science and Technology in Civil Engineering (JSTCE) - HUCE*, 19(3):54–68.

[6] Vo, T. P., Thai, H.-T., Nguyen, T.-K., Maheri, A., Lee, J. (2014). Finite element model for vibration and buckling of functionally graded sandwich beams based on a refined shear deformation theory. *Engineering Structures*, 64:12–22.

[7] Kahya, V., Turan, M. (2018). Vibration and stability analysis of functionally graded sandwich beams by a multi-layer finite element. *Composites Part B: Engineering*, 146:198–212.

[8] Liu, J., He, B., Ye, W., Yang, F. (2021). High performance model for buckling of functionally graded sandwich beams using a new semi-analytical method. *Composite Structures*, 262:113614.

[9] Van Vinh, P. (2021). Static bending analysis of functionally graded sandwich beams using a novel mixed beam element based on first-order shear deformation theory. *Forces in Mechanics*, 4:100039.

[10] Belarbi, M.-O., Houari, M. S. A., Hirane, H., Daikh, A. A., Bordas, S. P. A. (2022). On the finite element analysis of functionally graded sandwich curved beams via a new refined higher order shear deformation theory. *Composite Structures*, 279:114715.

[11] Garg, A., Chalak, H. D., Belarbi, M.-O., Zenkour, A. M. (2022). Hygro-thermo-mechanical based bending analysis of symmetric and unsymmetric power-law, exponential and sigmoidal FG sandwich beams. *Mechanics of Advanced Materials and Structures*, 29(25):4523–4545.

[12] Benzid, A., Tati, A. (2023). Static and buckling behaviors analysis of FG beams using a three unknowns finite element based on enhanced Timoshenko theory. *Mechanics of Advanced Materials and Structures*, 31(27):1–12.

[13] Gupta, S., Chalak, H. D. (2023). Buckling analysis of functionally graded sandwich beam based on third-order zigzag theory. *Mechanics of Advanced Composite Structures*, 10(1):55–68.

[14] Mesbah, A., Belabed, Z., Tounsi, A., Ghazwani, M. H., Alnujaie, A., Aldosari, S. M. (2024). Assessment of New Quasi-3D Finite Element Model for Free Vibration and Stability Behaviors of Thick Functionally Graded Beams. *Journal of Vibration Engineering & Technologies*, 12(2):2231–2247.

[15] Sayyidmousavi, A., Foroutan, M., Fawaz, Z. (2024). Meshfree dynamic analysis of functionally graded carbon nanotube reinforced polymer sandwich beams under harmonic moving loads. *Australian Journal of Mechanical Engineering*, 22(3):523–535.

[16] Li, J., Wang, G., Guan, Y., Zhao, G., Lin, J., Naceur, H., Coutellier, D. (2021). Meshless analysis of bi-directional functionally graded beam structures based on physical neutral surface. *Composite Structures*, 259:113502.

[17] Ahmadi, I. (2021). Vibration analysis of 2D-functionally graded nanobeams using the nonlocal theory and meshless method. *Engineering Analysis with Boundary Elements*, 124:142–154.

[18] Jiao, Z., Wang, G., Xu, R., Chen, W., Reddy, J. N. (2024). Free vibration and buckling analysis of functionally graded beams using the DMCDM. *Composite Structures*, 332:117905.

[19] Rahmani, F., Kamgar, R., Rahgozar, R. (2023). Analysis of metallic and functionally graded beams using isogeometric approach and Carrera Unified Formulation. *Mechanics of Advanced Materials and Structures*, 30(4):894–911.

[20] Dinachandra, M., Alankar, A. (2022). Static and dynamic modeling of functionally graded Euler–

Bernoulli microbeams based on reformulated strain gradient elasticity theory using isogeometric analysis. *Composite Structures*, 280:114923.

[21] Chen, D., Zheng, S., Wang, Y., Yang, L., Li, Z. (2020). Nonlinear free vibration analysis of a rotating two-dimensional functionally graded porous micro-beam using isogeometric analysis. *European Journal of Mechanics – A/Solids*, 84:104083.

[22] Trinh, D. T. N., Luong, K. A., Lee, J. (2024). An analysis of functionally graded thin-walled beams using physics-informed neural networks. *Engineering Structures*, 301:117290.

[23] Li, X.-F., Wang, B.-L., Han, J.-C. (2010). A higher-order theory for static and dynamic analyses of functionally graded beams. *Archive of Applied Mechanics*, 80:1197–1212.

[24] Pei, Y. L., Li, L. X. (2021). A simplified theory of FG curved beams. *European Journal of Mechanics – A/Solids*, 85:104126.

[25] Trinh, L. C., Vo, T. P., Osofero, A. I., Lee, J. (2016). Fundamental frequency analysis of functionally graded sandwich beams based on the state space approach. *Composite Structures*, 156:263–275.

[26] Karamanlı, A. (2018). Free vibration analysis of two directional functionally graded beams using a third order shear deformation theory. *Composite Structures*, 189:127–136.

[27] Nguyen, T.-K., Vo, T. P., Nguyen, B.-D., Lee, J. (2016). An analytical solution for buckling and vibration analysis of functionally graded sandwich beams using a quasi-3D shear deformation theory. *Composite Structures*, 156:238–252.

[28] Şimşek, M., Al-Shujairi, M. (2017). Static, free and forced vibration of functionally graded (FG) sandwich beams excited by two successive moving harmonic loads. *Composites Part B: Engineering*, 108: 18–34.

[29] Qin, B., Zhong, R., Wang, Q., Zhao, X. (2020). A Jacobi–Ritz approach for FGP beams with arbitrary boundary conditions based on a higher-order shear deformation theory. *Composite Structures*, 247: 112435.

[30] Balireddy, S. N., Pitchaimani, J., Mailan Chinnapandi, L. B. (2023). Acoustic response of bi-directional functionally graded beam under axially varying load. *Noise & Vibration Worldwide*, 54(10-11):512–526.

[31] Dash, S., Dey, T., Hati, D. (2024). Influence of thermo-mechanical loads on variable stiffness composite beams: a comprehensive study using semi-analytical and finite element approaches. *Mechanics Based Design of Structures and Machines*, 1–28.

[32] Nguyen, N.-D. (2025). Analysis of functionally graded porous curved beams with various boundary conditions. *International Journal of Mechanics and Materials in Design*, 1–24.

[33] Nguyen, N.-D., Bui, V.-T., Nguyen, V.-H., Vo, T. P. (2025). An analytical solution for comprehensive analysis of bio-inspired helicoidal laminated composite beams. *Journal of Reinforced Plastics and Composites*, page 07316844251356337.

[34] Shahgholian, D., Safarpour, M., Rahimi, A. R., Alibeigloo, A. (2020). Buckling analyses of functionally graded graphene-reinforced porous cylindrical shell using the Rayleigh–Ritz method. *Acta Mechanica*, 231(5):1887–1902.

[35] Xu, J., Gao, C., Li, H., Pang, F., Zheng, J., Hang, T. (2024). Jacobi–Ritz method for dynamic analysis of functionally graded cylindrical shell with general boundary conditions based on FSDT. *Computers & Structures*, 305:107552.

[36] Kiani, Y. (2016). Shear buckling of FG-CNT reinforced composite plates using Chebyshev–Ritz method. *Composites Part B: Engineering*, 105:176–187.

[37] Binh, C. T. (2025). Buckling analysis of GPL-reinforced FGM microplates using Pb-2 Ritz functions. *Journal of Science and Technology in Civil Engineering (JSTCE)-HUCE*, 19(2):119–132.

[38] Şimşek, M. (2010). Fundamental frequency analysis of functionally graded beams by using different higher-order beam theories. *Nuclear Engineering and Design*, 240(4):697–705.

[39] Nguyen, T.-K., Nguyen, T. T.-P., Vo, T. P., Thai, H.-T. (2015). Vibration and buckling analysis of functionally graded sandwich beams by a new higher-order shear deformation theory. *Composites Part B: Engineering*, 76:273–285.

[40] Mantari, J., Canales, F. (2016). Free vibration and buckling of laminated beams via hybrid Ritz solution for various penalized boundary conditions. *Composite Structures*, 152:306–315.

[41] Daneshvar, M. H., Gharighoran, A. R., Zareei, S. R., Jahangir, H., Rashidi, M. (2025). Utilizing Rayleigh–Ritz Technique to Identify Damages of Multi Span Beams. In *Damage Detection and Structural Health Monitoring of Concrete and Masonry Structures: Novel Techniques and Applications*, Springer, 199–206.

[42] Trinh, L. C., Nguyen, H. X., Vo, T. P., Nguyen, T.-K. (2016). Size-dependent behaviour of functionally graded microbeams using various shear deformation theories based on the modified couple stress theory. *Composite Structures*, 154:556–572.

## A. Appendix A [33]

$L_j(X)$ are the Laguerre Polynomials:

$$\begin{cases} L_0(X) = 1 \\ L_1(X) = 1 - X \\ L_{j+1}(X) = \left[(2j+1-X)L_j(X) - jL_{j-1}(X)\right]/(j+1) \end{cases} \qquad j = \overline{1,N} \tag{A.1}$$

## B. Appendix B [33]

$$\begin{aligned}
&K_{ij}^{11} = B_0 \int_0^L \Phi_{i,xx}\Phi_{j,xx}\,dx; \quad K_{ij}^{12} = -B_1 \int_0^L \Phi_{i,xx}\Phi_{j,xx}\,dx; \quad K_{ij}^{13} = B_3 \int_0^L \Phi_{i,xx}\Phi_{j,xx}\,dx \\
&K_{ij}^{22} = B_2 \int_0^L \Phi_{i,xx}\Phi_{j,xx}\,dx; \quad K_{ij}^{23} = -B_4 \int_0^L \Phi_{i,xx}\Phi_{j,xx}\,dx \\
&K_{ij}^{33} = B_5 \int_0^L \Phi_{i,xx}\Phi_{j,xx}\,dx + B_6 \int_0^L \Phi_{i,x}\Phi_{j,x}\,dx; \quad K_{Gij}^{22} = \int_0^L \Phi_{i,x}\Phi_{j,x}\,dx \\
&M_{ij}^{11} = J_0 \int_0^L \Phi_{i,x}\Phi_{j,x}\,dx; \quad M_{ij}^{12} = -J_1 \int_0^L \Phi_{i,x}\Phi_{j,x}\,dx; \quad M_{ij}^{13} = J_3 \int_0^L \Phi_{i,x}\Phi_{j,x}\,dx \\
&M_{ij}^{22} = J_0 \int_0^L \Phi_i\Phi_j\,dx + J_2 \int_0^L \Phi_{i,x}\Phi_{j,x}\,dx; \quad M_{ij}^{23} = -J_4 \int_0^L \Phi_{i,x}\Phi_{j,x}\,dx \\
&M_{ij}^{33} = J_5 \int_0^L \Phi_{i,x}\Phi_{j,x}\,dx; \quad F_i = \int_0^L q\Phi_i\,dx; \quad \mathbf{d} = \begin{bmatrix} w_{1j} & w_{3j} & \theta_j \end{bmatrix}^T
\end{aligned} \tag{B.1}$$